



**High-pressure structural systematics in samarium up to 222 GPa**S. E. Finnegan, E. J. Pace , C. V. Storm, and M. I. McMahon \**SUPA, School of Physics and Astronomy, and Centre for Science at Extreme Conditions, The University of Edinburgh, Peter Guthrie Tait Road, Edinburgh, EH9 3FD, United Kingdom*S. G. MacLeod *AWE, Aldermaston, Reading RG7 4PR, United Kingdom**and SUPA, School of Physics and Astronomy, and Centre for Science at Extreme Conditions, The University of Edinburgh, Peter Guthrie Tait Road, Edinburgh, EH9 3FD, United Kingdom*H.-P. Liermann  and K. Glazyrin *DESY, Notkestrasse 85, D-22607 Hamburg, Germany*

(Received 11 February 2020; revised manuscript received 9 April 2020; accepted 14 April 2020; published 15 May 2020)

Angle-dispersive x-ray powder diffraction experiments have been performed on samarium metal up to 222 GPa. Up to 50 GPa we observe the Sm type (*hR9*) → dhcp (*hP4*) → fcc (*cF4*) → distorted fcc (*hR24*) → *hP3* transition sequence reported previously. The structure of the high-pressure phase above 93 GPa, previously reported as having a monoclinic structure with space group *C2/m*, is found to be orthorhombic, space group *Fddd*, with eight atoms per unit cell (*oF8* in Pearson notation). This structure is the same as that found in Am, Cm, and Cf at high pressures. Analysis of samarium's equation of state reveals marked changes in compressibility in the *hP3* and *oF8* phases, with the compressibility of the *oF8* phase being that of a “regular” metal.

DOI: [10.1103/PhysRevB.101.174109](https://doi.org/10.1103/PhysRevB.101.174109)**I. INTRODUCTION**

The lanthanide series of elements is characterized by the monotonic filling of the *4f* electron shell, and the members of the series play an important role in many modern technologies, including high-performance permanent magnets, catalysts, and computer memories. As one traverses the series, the predominantly trivalent lanthanide elements (La to Lu, excluding Ce, Eu, and Yb) exhibit a reduction in their atomic radii, the well-known lanthanide contraction, and a change in the ambient-conditions crystal structure that correlates with changes in the *d*-band occupancy [1]. The same structural sequence—hcp → Sm type → dhcp → fcc → distorted fcc (*hP2* → *hR9* → *hP4* → *cF4* → *hR24* in Pearson notation)—can be induced via compression in individual lanthanide elements as a result of increased occupation of the *5d* states arising from pressure-induced *s*- to *d*-electron transfer [2,3]. The structures of all these phases comprise different stackings of close-packed or quasi-close-packed layers, and Raman scattering studies on Sm to 20 GPa [4] have reported that the structural sequence involves softening of optical and acoustic modes, implying also anomalies in the elastic behavior of the different phases. There are no measurable volume changes between the phases, but further compression of the *hR24* phase results in first-order phase transitions to the

so-called collapsed phases, the lower-symmetry structures of which have long been reported to arise from the participation of *4f* electrons in the bonding [5], although more recent studies have questioned this [6–9].

In Nd and Sm, the initial post-*hR24* phase is reported to be rhombohedral with space group *P3<sub>1</sub>21* and three atoms per unit cell (*hP3* in Pearson notation) and is obtained via a small volume change of ~0.4% [10]. On further compression, these two elements are then reported [11] to transform into a monoclinic structure (space group *C2/m*, *mC4* in Pearson notation) first observed in Ce at high pressure over 40 years ago [12]. The same *mC4* structure is reported in the collapsed phases of Gd, Tb, Dy, Ho, Er, and Tm, all of which are obtained via a direct first-order transition from the *hR24* phase rather than via the intermediate *hP3* phase [13–17].

We recently showed that the long-reported *mC4* structure is incorrect in Tb and also in Gd, Dy, Ho, Er, and Tm and that the true structure of these collapsed phases is orthorhombic, space group *Fddd*, with 16 atoms per unit cell (hereafter *oF16*) [18]. While isosymmetric with the eight-atom *Fddd* structure (hereafter *oF8*) found in Am, Cm, and Cf at high pressures [19–21], the *oF16* structure comprises an eight-layer ABCADCBD stacking of quasi-hcp layers, as opposed to the four-layer ABCD repeat seen in *oF8* (see Fig. 1). However, the nature of the stacking in the two structures is the same, with the atoms in each layer centered above the midpoint of two atoms in the previous layer, resulting in both having tenfold (6+2+2) coordination. We have also

\*m.i.mcmahon@ed.ac.uk

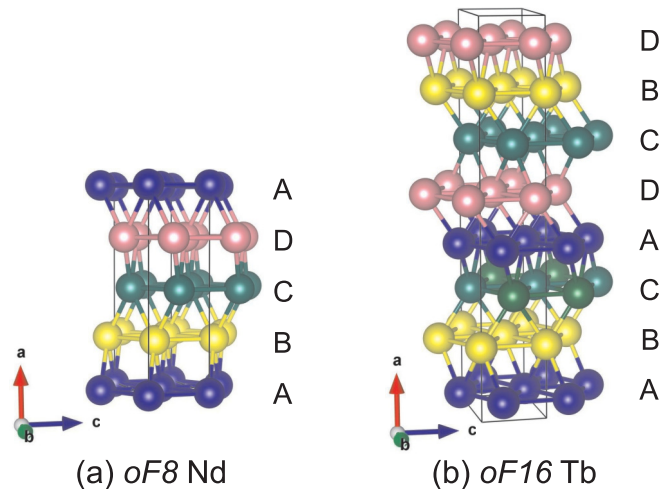


FIG. 1. The crystal structures of (a) *oF8*-Nd at 89 GPa and (b) *oF16*-Tb at 64 GPa. The structures are isosymmetric with the *Fddd* space group and differ in the stacking of their flat, hcp-like atomic layers: the stacking sequence in *oF8* is ABCD, while in *oF16* it is ABCADCBD.

reported that the *hP3* structure of Sm actually has space group  $P6_222$  rather than  $P3_121$  and that it has the same stacking as the *oF8* and *oF16* structures, although with a three-layer ABC stacking sequence [18]. Finally, we have noted that the reported diffraction profiles from the *mC4* phase of Nd [22] are remarkably similar to those from the *oF8* phase of Am, Cm, and Cf and that the published  $d$  spacings of Nd at 89 GPa [22] can be fitted perfectly with this orthorhombic structure [18]. The collapsed *oF8*, *oF16*, and *hP3* phases are thus all members of the same family of quasi-close-packed layer structures, differing only in the stacking sequence of the layers. The same structures are also seen in both the lanthanide and actinide elements.

The single trivalent lanthanide element whose high-pressure behavior does not seem to follow the same structural sequence is Sm [11]. While the post-*hP3* phase is reported to have the same *mC4* structure initially found in Nd [22], the reported diffraction patterns from Sm are dissimilar to those obtained from any other collapsed phase [11], including Nd, suggesting it has neither the *oF16* nor the *oF8* structure. To investigate whether Sm does, indeed, have a different sequence of high-pressure phases to any other lanthanide element, we have performed x-ray powder diffraction studies of Sm to 222 GPa. We find that the post-*hP3* phase does, indeed, have the same *oF8* structure seen in Nd, Am, Cm, and Cf and that this phase is stable to at least 222 GPa. We suggest that the diffraction pattern reported previously as coming from the *mC4* phase was, in fact, from a mixed-phase sample of *hP3* and *oF8*.

## II. EXPERIMENTAL DETAILS

High-purity distilled samples of Sm supplied by Ulrich Schwarz at the Max-Planck-Institut für Chemische Physik fester Stoffe in Dresden were loaded into three diamond-anvil cells (DACs) in a dry argon atmosphere ( $<1$  ppm  $O_2$  and  $<1$  ppm  $H_2O$ ) to prevent oxidation. The DACs were equipped

with beveled diamonds with 100- $\mu$ m culets and tungsten gaskets. The samples were loaded without any pressure medium but with a small copper sphere to act as a pressure calibrant, using the recently published Cu equation of state of Sokolova *et al.* [23].

Diffraction data were collected in two experiments on the Extreme Conditions P02.2 beamline at the PETRA III synchrotron in Hamburg and in a third experiment on the high-pressure I15 beamline at the Diamond Light Source (DLS) in the United Kingdom. Monochromatic x-ray beams with wavelengths of 0.2898 and 0.4808 Å (PETRA III) and 0.4248 Å (DLS), focused down to  $3 \times 6 \mu\text{m}^2$  and  $0.85 \times 0.85 \mu\text{m}^2$  (PETRA III) and  $20 \times 20 \mu\text{m}^2$  (DLS), were used, and the powder-diffraction data were recorded on Perkin-Elmer (PETRA-III) and Mar345 (DLS) area detectors, placed 300–400 mm from the sample.  $CeO_2$  and  $LaB_6$  diffraction standards were used to calibrate the exact sample-detector distances and the detector tilts. The two-dimensional diffraction patterns collected at each pressure were integrated azimuthally using FIT2D [24] and DIOPTAS [25] to obtain standard one-dimensional diffraction profiles, which were then analyzed using Rietveld and Le Bail methods or by fitting to the  $d$  spacings of individual diffraction peaks.

The submicron-diameter beam on the Extreme Conditions P02.2 beamline is a recent development ideally suited to high-pressure diffraction experiments above 200 GPa. The small beam minimizes parasitic scattering from the high- $Z$  metallic gasket surrounding the sample, minimizes pressure gradients in the diffracting sample volume, and also enables calibrant-free diffraction patterns to be obtained from the sample if required. Focusing is achieved by first cutting down the x-ray beam size  $\sim 35$  m from the source to approximately  $0.05 \times 0.05 \text{ mm}^2$  before using 136 Be compound refractive lenses [26], optimized for use at a fixed x-ray wavelength of 25.6 keV ( $\sim 0.48$  Å), to focus only the coherent part of the beam to  $0.85 \times 0.85 \mu\text{m}^2$  (FWHM) over a focal length of 360 mm (Fig. 2). Finally, the focused beam is passed through a 15- $\mu$ m-diameter pinhole immediately before the DAC in order to trim its tails. We have found that a 15- $\mu$ m pinhole provides the optimum trade-off between x-ray flux and the intensity of the parasitic scattering from the W gasket

## III. DISCUSSION

Diffraction patterns were first collected from the *hP3* phase below 50 GPa to ensure results consistent with those collected previously by Husband *et al.* [27]. The transition to the *hP3* phase was observed at 42(5) GPa, in excellent agreement with previous studies [27]. Analysis of the *hP3* patterns confirmed that the systematic absences were consistent with space group  $P6_222$  rather than  $P3_121$ .

On further compression above 50 GPa (see Fig. 3), evidence of the post-*hP3* phase was first observed at 93(4) GPa [Figure 3, profile (c)]. The peaks from the post-*hP3* phase increased in intensity on further compression [Figure 3, profiles (d)–(f)], and single-phase profiles were obtained above 157 GPa [Figure 3, profile (g)]. No further changes were observed up to 222(2) GPa, the highest pressure reached in this study.

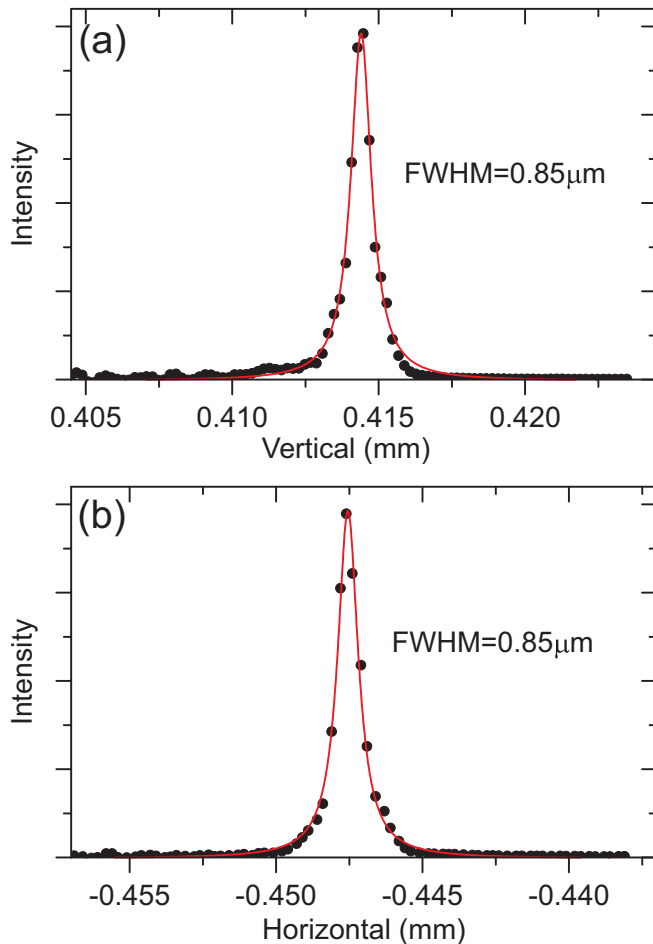


FIG. 2. Scans across the microfocused x-ray beam on the P02.2 beamline, both (a) vertically and (b) horizontally. The exact beam size in each direction varies from experiment to experiment but is typically  $0.85 \times 0.85 \mu\text{m}^2$  FWHM, as shown by the two Lorentzian curves.

The single-phase diffraction profiles obtained above 157 GPa are remarkably similar to those obtained from the *oF8* phase of Nd [22]. Figure 4 shows a Rietveld fit of the *oF8* structure to the diffraction profile from Sm at 175(2) GPa, where the refined lattice parameters are  $a = 8.4250(9) \text{ \AA}$ ,  $b = 4.5531(3) \text{ \AA}$ , and  $c = 2.5227(2) \text{ \AA}$  and  $V/V_0 = 0.364(2)$ , with atoms on the  $8a$  site at  $(0,0,0)$ . The fit is excellent, with all of the observed diffraction peaks being indexed.

The *oF8* structure of Sm and Nd and the *oF16* structure of Tb (see Fig. 1) both comprise stackings of flat, quasi-close-packed layers, the distortion of which from hexagonal symmetry can be quantified by the deviation of the  $b/c$  ratio from the ideal orthohexagonal value of  $\sqrt{3} = 1.732$ . The pressure dependence of the  $b/c$  ratio in *oF8*-Sm is shown in Fig. 5, along with the ideal value of  $\sqrt{3}$  in the *hP3* phase. There is a clear discontinuity in the “hexagonality” of the atomic layers from 1.732 to  $\sim 1.78$  at the *hP3*  $\rightarrow$  *oF8* transition, after which the distortion grows slowly and monotonically to reach a maximum value of 1.818(5) at 222 GPa. Our fit to the Nd diffraction pattern reported by Akella *et al.* at 89 GPa [22]

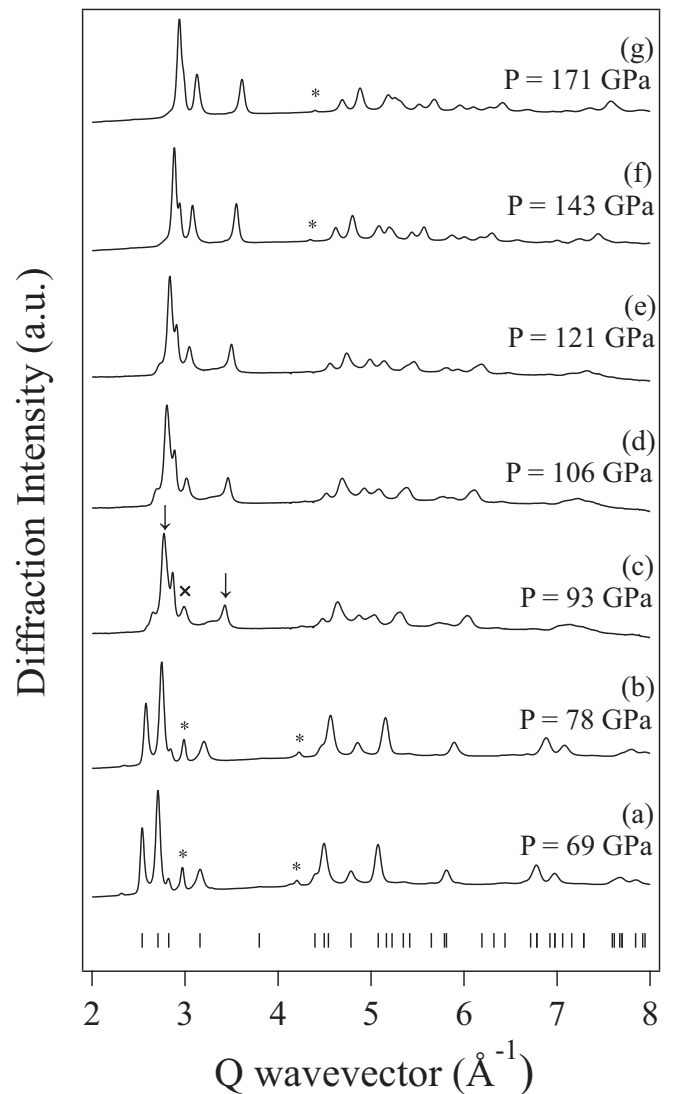


FIG. 3. Diffraction profiles collected from Sm on a pressure increase. The data were collected from the same sample during two different synchrotron visits and so are plotted as a function of wave vector  $Q$  in order to take into account the two different x-ray wavelengths used. Tick marks beneath profile (a) mark calculated peak positions from the *hP3* phase. The peaks marked with asterisks are from the W gasket. The arrows in profile (c) mark the first appearance of peaks from this phase. The reflections labeled with a cross in profile (c) indicate a doublet including the (101) peak from the W gasket and a peak from the post *hP3* phase. A single phase pattern of the post-*hP3* phase is seen in profile (g).

revealed a ratio of 1.7847(1) at that pressure [18], the same as that observed in *oF8*-Sm at  $\sim 132$  GPa.

The similarity of the *oF8*-Sm diffraction patterns reported here to those published previously from *oF8*-Nd above 75 GPa [22] raises the question of why the reported *mC4* structures from the two phases were previously very different [11,22]. However, it is clear that the diffraction pattern reported from Sm at 109 GPa [11] is not from a single-phase sample of *oF8*-Sm. Comparison of the 109 GPa diffraction pattern reported by Chesnut [11] with the mixed *hP3*-*oF8* profile obtained in the current study at 106 GPa [see Fig. 3,

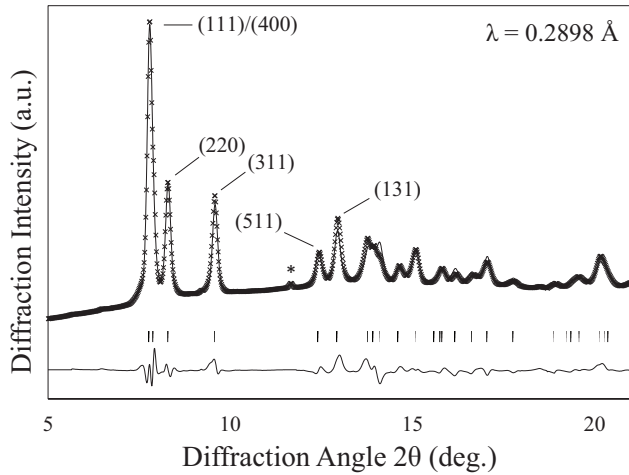


FIG. 4. Rietveld refinement of the *oF8* structure to a diffraction profile from Sm at 175 GPa, showing the observed (crosses) and calculated (line) diffraction patterns, the calculated reflection positions, and the difference profile ( $R_p = 2.1\%$ ,  $R_{wp} = 3.1\%$ ,  $R_E = 2.8\%$ , goodness of fit (GoF) = 1.09, and  $R(F^2) = 7.2\%$ ). The first six peaks of the *oF8* phase are labeled with their Miller indices, and the asterisk identifies the (200) peak from the W gasket [the (110) peak from the gasket is overlapped by the (220) reflection from Sm].

profile (d)] reveals them to be very similar. A two-phase *hP3*-*oF8* Le Bail fit to this profile is shown in Fig. 6, which reveals that all of the observable peaks are explained by the two-phase model. We therefore suspect that Chesnut's analysis at 109 GPa was hampered by the use of a profile

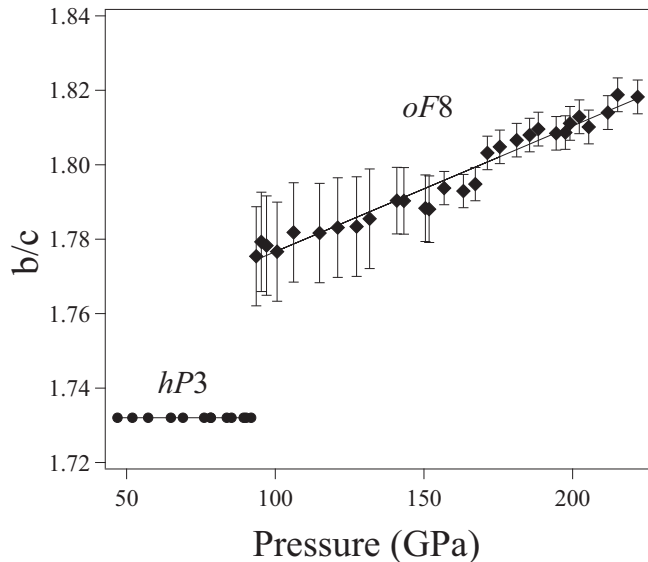


FIG. 5. The pressure dependence of the hexagonality of the atomic layers in the *oF8* phase of Sm. The distortion in the *oF8* phase can be quantified by the deviation of the  $b/c$  ratio from the ideal orthohexagonal value of  $\sqrt{3}$  (1.732). The atomic layers in the *hP3* phase have perfect hexagonal symmetry and hence have the ideal orthohexagonal value. The discontinuity in the geometry of the layers at the *hP3*  $\rightarrow$  *oF8* transition at 93 GPa is very clear and suggests that the transition is not continuous.

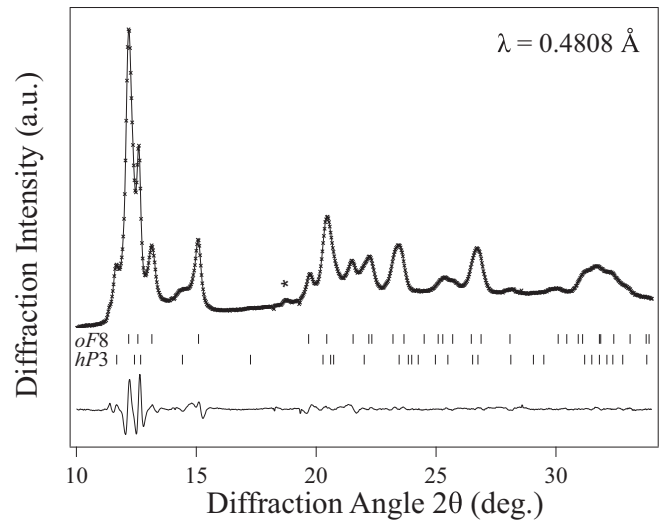


FIG. 6. Le Bail fit of the *hP3* and *oF8* structures to a mixed-phase diffraction profile from Sm at 106 GPa, showing the observed (crosses) and calculated (line) diffraction patterns, the calculated peak positions of the two phases, and the difference profile. The asterisk identifies the (200) peak from the W gasket. This is the same profile as that shown in Fig. 3(d).

from a mixed-phase sample. Unfortunately, while that study attained pressures of 200 GPa, where single-phase patterns from the *oF8* phase might be expected, no diffraction profiles were shown above 109 GPa.

The compressibility of Sm to 222 GPa, including the data of Husband *et al.* below 50 GPa [27], is shown in Fig. 7. The similarities of the *hP3* and *oF8* structures, which differ only in the stacking sequence of their hcp-like layers [18], result in a sizable pressure range (for example, 93–157 GPa in one of our samples; see Fig. 3) over which mixed *hP3*-*oF8* profiles are observed and in extensive peak overlap in this

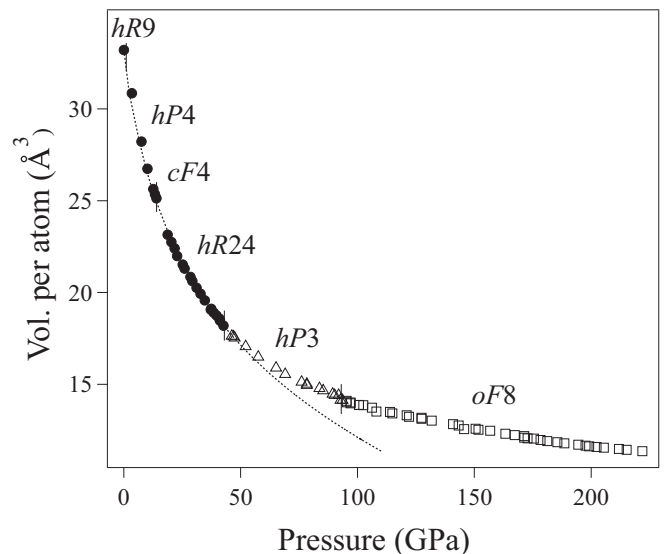


FIG. 7. The compressibility of Sm up to 222 GPa. The dotted line shows the AP2 equation of state obtained from fitting the data to 43 GPa. The misfit beyond 43 GPa can be clearly observed.

mixed-phase region. The  $P6_22$  and  $Fddd$  space groups are not group-subgroup related, and so the transition between the  $hP3$  and  $oF8$  structures need not be second order. Indeed, the sharp discontinuity observed in the geometry of the atomic layers at the  $hP3 \rightarrow oF8$  transition (Fig. 5) suggests that the transition is not continuous. However, careful analysis of mixed-phase profiles reveals that there is no measurable volume change at the transition, despite the discontinuity in the shape of the atomic layers.

Fits to the compression data of Sm up to 43 GPa (that is, up to the  $hR24 \rightarrow hP3$  transition) were made with the second-order (AP2) form of the adapted polynomial of order  $L$  (APL) equation of state (EOS) [28]

$$P = 3K_0 \frac{(1-x)}{x^5} \exp[c_0(1-x)] \left[ 1 + x \sum_{k=2}^L c_k (1-x)^{k-1} \right], \quad (1)$$

where  $K_0$  is the zero-pressure bulk modulus,  $K'$  is its pressure derivative,  $x = (V/V_0)^{1/3}$ ,  $c_0 = -\ln(3K_0/p_{FG})$ ,  $c_2 = (3/2)(K' - 3) - c_0$ ,  $p_{FG} = a_{FG}(Z/V_0)^{5/3}$  is the Fermi-gas pressure,  $Z$  is the atomic number, and  $a_{FG} = [(3\pi^2)/5](\hbar^2/m_e) = 0.02337 \text{ GPa nm}^5$  is a constant. This gave an excellent fit with  $K_0 = 33.4(5) \text{ GPa}$  and  $K' = 3.08(3)$  [29] (see Fig. 7). However, extrapolation of this EOS to higher pressures revealed an increasingly poor fit, with the compressibilities of both the  $hP3$  and  $oF8$  phases above 43 GPa being considerably smaller than that predicted from the extrapolation of the AP2 EOS obtained from the data below that pressure (see Fig. 7).

Fits to the full compression curve to 222 GPa using a single AP2 EOS were poor, and the inability of second-order EOSs to fit the Sm compression curve was noted previously by both Zhao *et al.* [30] and Chesnut [11], who subsequently fitted third-order Birch and modified universal EOSs, respectively, to their data. Anomalies in the EOS data for the individual phases of Sm can be most readily visualized by using a simple “linearization” procedure whereby anomalies arising from changes in electronic structure can be distinguished from the “normal” compressive behavior of regular metals [31].

Figure 8 shows the APL linearized compression data for Sm in the form of a  $\eta_{APL} - x$  plot,

$$\eta_{APL}(x) = \ln(px^5/p_{FG}) - \ln(1-x), \quad (2)$$

where  $x = (V/V_0)^{1/3}$ ,  $p_{FG} = a_{FG}(Z/V_0)^{5/3}$ , and  $a_{FG} = 0.02337 \text{ GPa nm}^5$ , along with similarly linearized data for the “regular” metals Au and Pt [32]. In such a plot, materials undergoing normal compression will show linear or quasilinear behavior, with the correct theoretical limit of  $\eta(0) = 0$  at  $x = 0$ . The behavior of Au and Pt clearly exhibits this form. In marked contrast to the very linear behavior of Au and Pt, the data for Sm exhibit significant curvature, as noted previously by Zhao *et al.* for Sm [30] and by Grosshans and Holzapfel [33] for the trivalent lanthanides in general, and there is a clear change in gradient after the  $hR24$  to  $hP3$  transition at 43 GPa ( $x \sim 0.81$ ) such that above 65 GPa ( $x \sim 0.78$ ) the data from the  $hP3$  and  $oF8$  phases show normal linear behavior, extrapolating to  $\eta(0) \sim 0$ . The  $oF8$  phase of Sm might then be regarded as a regular metal.

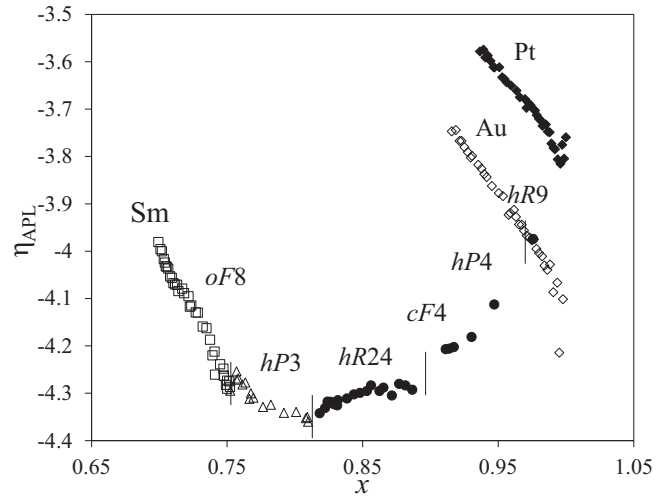


FIG. 8. Linearization of the compression of Sm shown in the form of an  $\eta_{APL}-x$  plot. The data from the different phases of Sm are plotted using different symbols, and the “regular” compressibilities of Au and Pt, as calculated from the compression data of Dewaele *et al.* [32], are shown for comparison.

Zhao *et al.* drew attention to these changes in gradient using their data collected over a smaller compression range and using the incorrect structure for Sm above 90 GPa and suggested that they arose from the change in the nature of the bonding in the different phases: from  $d$  bonding in  $hR24$  to intermediate  $4f$  bonding in  $hP3$  to itinerant  $4f$  bonding in the  $oF8$  phase [30]. The valence state of Yb metal has long been known to change on pressure increase [34,35], and Herbst and Wilkins [36] predicted a valence transition in Sm from  $3+$  to  $2+$  at  $\sim 100$  GPa, close to the  $hP3 \rightarrow oF8$  transition pressure of 92 GPa. Such a divalent state is reported to contribute to the high-temperature magnetic susceptibility of Sm at ambient pressure [37]. Any valence change might be expected to have an effect on the compressibility of Sm, but as shown in Fig. 8, there is no change in behavior at the  $hP3 \rightarrow oF8$  transition. Recent  $L_3$  x-ray appearance near-edge structure measurements on Tb to 65 GPa [38] and on Dy to 115 GPa [39] explicitly ruled out the presence of a valence transition in either of these higher-Z lanthanide elements at high pressure. Similar studies are required on Sm to see if it too remains trivalent to the highest pressures.

The data shown by Zhao *et al.* were from a variety of sources and exhibited considerable scatter and, as mentioned, used an incorrect structure for the  $oF8$  phase. Our data, collected from three samples of the same ingot, the pressures for which were obtained using the same Cu EOS, show greater consistency, and the changes in gradient in the linearized plot are therefore clearer. Our data to 222 GPa suggest that the discontinuity in incompressibility occurs between 45 and 65 GPa within the  $hP3$  phase, with no further change being observed at the  $hP3 \rightarrow oF8$  transition at 93 GPa.

As mentioned previously, both Zhao *et al.* [30] and Chesnut [11] found that third-order EOSs provided a better fit to their data, and Fig. 9 shows the fit [29] of a third-order APL (AP3) EOS to the full Sm compression curve with  $K_0 = 40.6(11) \text{ GPa}$ ,  $K' = 1.58(6)$ , and  $K'' = -0.0524(3)$ . While

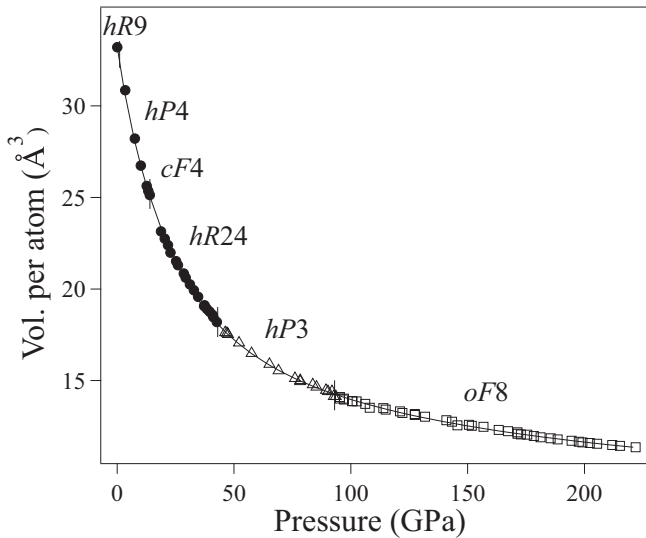


FIG. 9. The compressibility of Sm up to 222 GPa. The solid line shows the best-fitting third-order AP3 EOS to the full compression curve.

the AP3 form fits the full compression curve much better than the AP2 form, the  $K_0$  value of 40.6 GPa is larger than the value of 31.6 GPa obtained by fitting only the data up to 43 GPa and the value of 33 GPa reported previously [33]. Close analysis of the AP3 fit reveals that it slightly underestimates the compressibility of the lower-pressure ( $hR9$ ,  $hP4$ ,  $cF4$ , and  $hR24$ ) phases to 43 GPa (and therefore overestimates  $K_0$ ) in order to better fit the higher-pressure ( $hP3$  and  $oF8$ ) phases over the larger pressure range of 43 to 222 GPa.

For many regular solids, such as the  $oF8$  phase of Sm above 93 GPa,  $c_2$  and all the higher-order terms  $c_k$  ( $k > 2$ ) of the APL EOS [see Eq. (1)] are zero [40], which implies, for the corresponding AP1 form, that

$$K'_{AP1} = 3 + (2/3)c_0. \quad (3)$$

The AP1 form thus has only two variables ( $V_0$  and  $K_0$ ), and it has been used to fit compression data from high-pressure phases when the pressure values for the first data points from that phase are small relative to the total pressure range for data for that phase [40]. Despite having no data below 93 GPa, the 100+ GPa pressure range over which we have compression data for the  $oF8$  phase meant that fitting the AP1 EOS to the  $oF8$  phase was straightforward, giving values of  $V_0 = 37.9(7) \text{ \AA}^3/\text{atom}$ ,  $K_0 = 4.0(4) \text{ GPa}$ , and  $K' = 7.07(6)$ . Since the  $oF8$  phase is unstable at low pressures, there is no experimental value of  $V_0$  with which to compare the fitted value. However, the *calculated* value for this phase at ambient pressure and 0 K, as obtained from electronic structure calculations, is  $35.95 \text{ \AA}^3/\text{atom}$  [41]. Fixing  $V_0$  at this calculated value, the AP1 fit gave  $V_0 = 35.95 \text{ \AA}^3/\text{atom}$  (fixed),  $K_0 = 5.08(1) \text{ GPa}$ , and  $K' = 6.96(2)$ , values not too dissimilar from those obtained from the free fit. While the small value of  $K_0$  is that of an alkali metal, such as potassium ( $K_0 = 3.1 \text{ GPa}$ ) or sodium ( $K_0 = 6.3 \text{ GPa}$ ), the large value of  $K'$  results in a bulk modulus of  $\sim 390 \text{ GPa}$  for the  $oF8$  phase at 95 GPa

Low-temperature magnetic studies of Sm to 50 GPa have shown that the magnetic transition temperatures closely follow the crystallographic symmetry during the  $hR9 \rightarrow hP4 \rightarrow cF4 \rightarrow hR24$  transition sequence at high pressures and low temperatures [42]. More recently, Deng and Schilling measured the magnetic ordering temperature  $T_0$  of Sm metal up to 150 GPa and observed a strong increase in  $T_0$  with pressure above 85 GPa from  $\sim 60$  to  $\sim 140 \text{ K}$  [9]. This pressure is close to that of the  $hP3 \rightarrow oF8$  transition in Sm at 300 K, and so it is likely that it is the  $oF8$  phase of Sm that has a highly correlated electron state, such as a Kondo lattice [9]. Given the very similar structural behavior of Nd and Sm reported here, it is perhaps then surprising that the magnetic ordering temperature  $T_0$  of Nd *decreases* sharply from 180 to 120 K between 70 and 110 GPa, where it has the  $oF8$  structure at 300 K, before decreasing toward 0 K near 150 GPa [6]. Electronic structure calculations are needed both to cast light on the different magnetic behaviors seen in Sm and Nd and to determine why the  $oF16$  structure of Tb and the higher-Z trivalent lanthanides is not seen in either Sm or Nd.

#### IV. CONCLUSIONS

The structure of Sm metal above 93 GPa is found to be face-centered orthorhombic ( $oF8$ ), isostructural with that observed in Nd, Am, Cm, and Cf at high pressures, and isosymmetric with the  $oF16$  structure observed in Tb, Gd, Dy, Ho, Er, and (probably) Tm [18]. High-precision measurements of the compressibility of Sm reveal that it becomes less compressible after the transition to the  $hP3$  phase at 43 GPa and that above 65 GPa its compressibility is that of a regular metal such as Au or Pt. Previous studies of Sm have linked changes in its crystal structure and compressibility to changes in its electronic structure, particularly changes from  $d$  bonding in the  $hR24$  structure to intermediate  $4f$  bonding in the  $hP3$  structure to itinerant  $4f$  bonding in the  $oF8$  structure. Previous calculations which have suggested a delocalization of the  $4f$  shell in the 100-GPa pressure range were performed on the assumption that the post- $hP3$  phases of Sm has a body-centered tetragonal structure ( $tI2$ ) rather than the  $oF8$  structure reported here [43]. Further calculations using the correct crystal structure are therefore now required.

#### ACKNOWLEDGMENTS

British Crown Owned Copyright 2020/AWE. Published with permission of the Controller of Her Britannic Majesty's Stationery Office. This work was supported by grants (Grants No. EP/R02927X/1 and No. EP/R02992X/1) from the U.K. Engineering and Physical Sciences Research Council (EPSRC) and experimental facilities made available by DESY (Hamburg, Germany), a member of the Helmholtz Association HGF, and by the Diamond Light Source (DLS). The research leading to this result has been supported by the project CALIPSOplus under the Grant Agreement 730872 from the EU Framework Programme for Research and Innovation HORIZON 2020. We would like to thank R. J. Husband for her assistance on beamline P02.2 at PETRA III and D. Daisenberger for his support on the I15 beamline at DLS. S.E.F. and C.V.S. are grateful to AWE for the award of CASE

studentships. We would like to thank R. J. Angel for revising his EOSFIT code in order to be able to fit both the AP2 and AP3 equations of state to our compression data. Finally, the

preparation of this paper has benefited greatly from many discussions with W. B. Holzapfel about the APL equations of state.

- 
- [1] J. C. Duthie and D. G. Pettifor, *Phys. Rev. Lett.* **38**, 564 (1977).
- [2] B. Johansson and A. Rosengren, *Phys. Rev. B* **11**, 2836 (1975).
- [3] D. A. Young, *Phase Diagrams of the Elements* (University of California Press, Berkeley, CA, 1991).
- [4] H. Olijnyk and A. P. Jephcoat, *Europhys. Lett.* **69**, 385 (2005).
- [5] B. Johansson and A. Rosengren, *Phys. Rev. B* **11**, 1367 (1975).
- [6] J. Song, W. Bi, D. Haskel, and J. S. Schilling, *Phys. Rev. B* **95**, 205138 (2017).
- [7] J. Lim, G. Fabbris, D. Haskel, and J. S. Schilling, *Phys. Rev. B* **91**, 174428 (2015).
- [8] J. Lim, G. Fabbris, D. Haskel, and J. S. Schilling, *Phys. Rev. B* **91**, 045116 (2015).
- [9] Y. Deng and J. S. Schilling, *Phys. Rev. B* **99**, 085137 (2019).
- [10] R. J. Husband, Ph.D. thesis, The University of Edinburgh, 2015.
- [11] G. N. Chesnut, Ph.D. thesis, The University of Alabama at Birmingham, 2002.
- [12] W. H. Zachariasen, *Proc. Natl. Acad. Sci. USA* **75**, 1066 (1978).
- [13] D. Errandonea, R. Boehler, B. Schwager, and M. Mezouar, *Phys. Rev. B* **75**, 014103 (2007).
- [14] N. C. Cunningham, W. Qiu, K. M. Hope, H.-P. Liermann, and Y. K. Vohra, *Phys. Rev. B* **76**, 212101 (2007).
- [15] G. K. Samudrala, S. A. Thomas, J. M. Montgomery, and Y. K. Vohra, *J. Phys.: Condens. Matter* **23**, 315701 (2011).
- [16] J. M. Montgomery, G. K. Samudrala, G. M. Tsoi, and Y. K. Vohra, *J. Phys.: Condens. Matter* **23**, 155701 (2011).
- [17] G. K. Samudrala and Y. K. Vohra, in *Handbook on the Physics and Chemistry of Rare Earths* (Elsevier, Amsterdam, The Netherlands, 2013), vol. 43, pp. 275–319.
- [18] M. I. McMahon, S. Finnegan, R. J. Husband, K. A. Munro, E. Plekhanov, N. Bonini, C. Weber, M. Hanfland, U. Schwarz, and S. G. Macleod, *Phys. Rev. B* **100**, 024107 (2019).
- [19] S. Heathman, R. G. Haire, T. Le Bihan, A. Lindbaum, K. Litfin, Y. Méresse, and H. Libotte, *Phys. Rev. Lett.* **85**, 2961 (2000).
- [20] S. Heathman, R. G. Haire, T. Le Bihan, A. Lindbaum, M. Idiri, P. Normile, S. Li, R. Ahuja, B. Johansson, and G. H. Lander, *Science* **309**, 110 (2005).
- [21] S. Heathman, T. Le Bihan, S. Yagoubi, B. Johansson, and R. Ahuja, *Phys. Rev. B* **87**, 214111 (2013).
- [22] J. Akella, S. T. Weir, Y. K. Vohra, H. Prokop, S. A. Catledge, and G. N. Chesnut, *J. Phys.: Condens. Matter* **11**, 6515 (1999).
- [23] T. S. Sokolova, P. I. Dorogokupets, A. M. Dymshits, B. S. Danilova, and K. D. Litasov, *Comput. Geosci.* **94**, 162 (2016).
- [24] A. P. Hammersley, S. O. Svensson, M. Hanfland, A. N. Fitch, and D. Häusermann, *High Pressure Research* **14**, 235 (1996).
- [25] C. Prescher and V. B. Prakapenka, *High Press. Res.* **35**, 223 (2015).
- [26] A. Snigirev, V. Kohn, I. Snigireva, and B. Lengeler, *Nature (London)* **384**, 49 (1996).
- [27] R. J. Husband, I. Loa, K. Munro, and M. I. McMahon, *J. Phys.: Conf. Ser.* **500**, 032009 (2014).
- [28] W. B. Holzapfel, *High Pressure Res.* **16**, 81 (1998).
- [29] R. J. Angel, M. Alvaro, and J. Gonzalez-Platas, *Z. Kristallogr. - Cryst. Mater.* **229**, 405 (2014).
- [30] Y. C. Zhao, F. Porsch, and W. B. Holzapfel, *Phys. Rev. B* **50**, 6603 (1994).
- [31] W. B. Holzapfel, in *Correlations in Condensed Matter under Extreme Conditions* (Springer, Cham, 2017), pp. 91–106.
- [32] A. Dewaele, P. Loubeyre, and M. Mezouar, *Phys. Rev. B* **70**, 094112 (2004).
- [33] W. A. Grosshans and W. B. Holzapfel, *Phys. Rev. B* **45**, 5171 (1992).
- [34] K. Syassen, G. Wortmann, J. Feldhaus, K. H. Frank, and G. Kaindl, *Phys. Rev. B* **26**, 4745 (1982).
- [35] A. Fuse, G. Nakamoto, M. Kurisu, N. Ishimatsu, and H. Tanida, *J. Alloys Compd.* **376**, 34 (2004).
- [36] J. F. Herbst and J. W. Wilkins, *Phys. Rev. B* **29**, 5992 (1984).
- [37] N. S. Uporova, S. A. Uporov, and V. E. Sidorov, *J. Exp. Theor. Phys.* **114**, 281 (2012).
- [38] G. Fabbris, T. Matsuoka, J. Lim, J. R. L. Mardegan, K. Shimizu, D. Haskel, and J. S. Schilling, *Phys. Rev. B* **88**, 245103 (2013).
- [39] J. S. Schilling, in *Correlations in Condensed Matter under Extreme Conditions: A Tribute to Renato Pucci on the Occasion of His 70th Birthday*, edited by G. G. N. Angilella and A. La Magna (Springer, Cham, 2017), pp. 47–56.
- [40] W. B. Holzapfel, *Rev. High Pressure Sci. Technol.* **11**, 55 (2001).
- [41] E. Plekhanov, N. Bonini, and C. Weber (unpublished).
- [42] C. R. Johnson, G. M. Tsoi, and Y. K. Vohra, *J. Phys.: Condens. Matter* **29**, 065801 (2016).
- [43] P. Söderlind, O. Eriksson, J. M. Wills, and A. M. Boring, *Phys. Rev. B* **48**, 5844 (1993).